An EBSD study of the deformation of service-aged 316 austenitic steel

Journal Item

An EBSD study of the deformation of service-aged 316 austenitic steel

D N Githinji*, S M Northover, P J Bouchard, M Rist†

Materials Engineering, The Open University, Walton hall, Milton Keynes, MK7 6AA, UK

* Corresponding author, Tel.: +44(0)1908 858169 ext. 53594, Email: d.n.githinji@open.ac.uk

Abstract

Electron backscatter diffraction (EBSD) has been used to examine the plastic deformation of an ex-service 316 austenitic stainless steel at 297K and 823K at strain rates $3.5x10^{-3}s^{-1}$ – $4x10^{-7}s^{-1}$. The distribution of local misorientations was found to depend on the imposed plastic strain following a lognormal distribution at true strains < 0.1 and a gamma distribution at strains > 0.1. At 823K the distribution of misorientations depended on the applied strain rate. The evolution of lattice misorientations with increasing plastic strain up to 0.23 was quantified using the metrics kernel average misorientation, average intragrain misorientation, and low angle misorientation fraction. For strain rate down to $10^{-5}s^{-1}$ all metrics were insensitive to deformation temperature, mode (tension vs. compression) and orientation of the measurement plane. The strain sensitivity of the different metrics was found to depend on the misorientation ranges considered in their calculation. A simple new metric, proportion of undeformed grains, is proposed for assessing strain in both aged and unaged material. Lattice misorientations build up with strain faster in aged steel than in un-aged material and most of the metrics were sensitive to the effects of thermal aging. Ignoring aging effects leads to significant overestimation of the strains around welds. The EBSD results were compared with nanohardness measurements and good agreement established between the two techniques of assessing plastic strain in aged 316 steel.

Keywords

Austenitic stainless steel; Plastic deformation; Electron backscatter diffraction; Strain rate; Misorientation distribution; Hardness;

1. Introduction

AISI type 316 austenitic stainless steel is widely used in power plants because of its good high temperature strength, oxidation and creep resistance [1, 2] but long term exposure to temperatures above 823K during service can degrade its mechanical properties [3] and plastic strain can increase its susceptibility to stress corrosion cracking [4-6]. Predictions of a plant's remaining safe operating life require reliable methods of determining the inelastic strain levels already reached in safety critical 316 steel components and good models of the operative deformation mechanisms. Measurements of strain distributions around welds made in already aged material are of particular interest because welded repairs may be necessary after several years of plant operation.

Electron backscatter diffraction (EBSD) has been used to measure plastic strain in various metals including solution annealed (SA) 316 steel [7-10] and several different EBSD metrics have been observed to scale with strain in the same way for both compressive and tensile strain. The metric grain average misorientation (GAM) has shown promise for evaluating creep damage in SA material [7-10] but there have been no EBSD studies on ex-service (aged) material where copious intragranular and intergranular precipitation might be expected to change the deformation behavior. There have also been no studies of whether EBSD measurements are sensitive to changes in deformation that may arise through changes in temperature or strain rate. This paper describes the results of an experimental study of deformation of AISI Type 316H steel which had previously seen long term service at high temperatures (~789K) using EBSD to follow the build up of intragranular misorientations with applied strain (both tensile and compressive) at different temperatures and strain rates. It compares the application of three different established EBSD metrics to the measurement of plastic strain in steel with well-developed precipitation and proposes a simple new metric that can be applied to both aged and non-aged material.

1.1. *Strain measurement using EBSD*

In EBSD a fine beam of electrons is focused sequentially on a grid of points on the surface of a crystalline material. Diffraction of the electrons backscattered from the top 10-100nm [11, 12] forms patterns from which the crystallographic orientation of the material under each spot can be determined. The generation and accumulation of dislocations during metal's plastic deformation results in local changes to the lattice orientation and plastic strain can be estimated by measuring these local orientation differences (misorientations). The dislocations which contribute to the lattice rotations are known as geometrically necessary dislocations (GNDs) [13]. Plastic strain also degrades the quality of the diffraction patterns and this effect has also been used to estimate plastic strain e.g.[8, 14] but this approach suffers from the disadvantage that many other factors such as surface contamination, surface preparation, pattern overlap close to grain boundaries, compositional variations and the particular crystallographic planes contributing to an individual pattern [15] affect the pattern quality too and may give misleading results.

The accuracy of strain assessment by measuring local misorientations clearly depends on the accuracy with which each individual orientation can be determined which in turn depends on the microscope operating conditions, the pattern acquisition parameters and the condition of the surface [16].

The use of various EBSD metrics for the analysis of plastic strain has recently been reviewed [17] but there is little published work concerning the behavior of these metrics after deformation at different temperatures, strain rates and deformation mode. Most work in this area has focused on the development of calibration curves for solution treated materials [7-10, 18-20] based on room temperature deformation. The use of such curves in assessing plastic strain developed at high temperatures is limited by differences in the deformation mechanisms operating at different temperatures and by the effects of microstructural changes

occurring during high temperature deformation. These include the development of intragranular and intergranular precipitation and changes in the grain size distribution which alter the deformation behavior from that of the SA material. The influence of aging on the ‘ Low angle boundary fraction (LABF)’ [17] EBSD metric has been demonstrated in a ferritic steel [21] which showed LABF in unstrained P91 steels to vary with aging time at 923K, but there have been no systematic studies on aged austenitic steel investigating the behavior of the various metrics after different deformations.

The metric Integrated Angular Misorientation Density (IMD) , which is based on spatially correlated misorientations, has been found to have a close to linear relationship with applied plastic strain under both compressive and tensile deformations at room temperature although the two different deformation modes gave different IMD values at any given strain level [22]. There has been no examination of whether the observed non-linear behavior of other metrics e.g. [23] with increasing strain beyond 0.15-0.2 are the result of a change in the underlying dislocation behavior or result from the way each metric is defined and calculated. There is little literature on the effects of deformation strain rate on EBSD. This has been addressed indirectly [10 , 23, 24] by comparing results obtained from uniaxial tensile and from creep tests but there have been no systematic studies in which strain rate was the only variable.

Several studies [8, 10, 25-27] have demonstrated good correlation between hardness and different EBSD metrics, implying a relationship between the metrics and the overall dislocation density rather than its relating solely to the density of GNDs. Thus hardness can provide a comparison for EBSD measurements of strain, although with the reservation that the volume of the strain fields sampled by the two techniques differs by several orders of magnitude. In this study, the EBSD metrics investigated were kernel averaging misorientation (KAM), average intragrain misorientation (AMIS), low angle misorientation

fraction (LAMF)[1]and, a new metric, proportion of undeformed grains (PUG). The sensitivity of the metrics is examined under different deformation conditions and a statistical approach adopted to determine the nature of their variations with the applied plastic strain.

1.2. *Validity of EBSD measurement of misorientations and bulk plastic strain*

Since EBSD measurements are made from a layer of material less than 100nm from the surface this can only be typical of the bulk strain if the local misorientations in this layer are representative of those below. Although dislocation dynamics simulations for Cu suggest that dislocations relax within 65nm of a free surface, comparisons between EBSD measurements and those from X-ray microdiffraction (which probed to a depth ~ 2μm) on a Cu single crystal deformed to a macroscopic strain of about 0.1 showed very similar overall lattice rotations measured by each technique [28] which gives confidence that, although a surface technique, EBSD can give reliable information about deformation in the bulk.

2. Material and Experimental Procedures

2.1. *Material*

AISI Type 316H austenitic stainless steel supplied by EDF Energy was used in this study. The steel which was part of a power plant steam header had been in service for 90,930 hours at about 789K and its composition (weight percentage) was given as C-0.07%, Si-0.41%, Mn-0.98%, P-0.024%, S-0.016%, Cr-17.2%, Ni-11.5%, Mo-2.3%, Al-0.003%, As-0.01, Cu-0.14%, Pb-0.002%, Sn-0.011%, V-0.04%, W-0.05%, Co-0.07%, N-0.03%, Sb <0.01%, Nb <0.005% , Ti <0.01% and Fe balance. The average grain size of the steel was 98±10μm and there was extensive intragranular and intergranular precipitation as shown in Fig. 1. Tubes of solution annealed AISI 316H steel of 30μm grain size and composition given as C-0.05%,

[1] Although generally referred to in the literature as LABF, in this work the metric based on the detection by the EBSD processing software of misorientations between adjacent measurement points >2 ^{o} and <15^{o} will be referred to as low angle misorientation fraction (LAMF) because the misorientations concerned do not necessarily arise from the presence of a low angle boundary but more frequently by the gradual accumulation of misorientation over the distance between adjacent measurement points.

Si-0.53%, Mn-1.55%, P-0.029%, S-0.005%, Cr-16.89%, Ni-11.25%, Mo-2.04%, Co-0.089% and Fe balance were also included in the study.

2.2. *Experimental procedures*

2.2.1. Mechanical tests

A summary of the mechanical tests performed is given in Table 1. The tests included room temperature tensile (RTT), high temperature tensile (HTT), room temperature compression (RTC), high temperature compression (HTC) and high temperature strain rate tests (HTST). Tensile specimens of 6mm diameter and 30mm gauge length were extracted from the aged steel by electric discharge machining (EDM) and deformed uniaxially on an Instron-8862 machine under the conditions given in Table1. Four specimens (SARTT) were solution annealed for 1hour at 1323K and tested as given in Table1. Compression specimens 10 mm in diameter and 15 mm long were also extracted from the aged steel and deformed uniaxially on an MTS-810 servo-hydraulic machine under the conditions given in Table 1. The HTT, HTC and HTST specimens were heated to about 823K and held for 1 hour to allow temperature homogenization before being deformed. The strain was measured using an extensometer attached directly onto the specimen's gauge length except for HTC tests where the strain was calculated from the axial displacement of machine's crosshead. Molybdenum disulphide (MoS_2) and boron nitride based lubricants were used in the room and high temperature compression tests, respectively, to reduce the contact friction between the specimen and the machine's platens and thus the specimen's tendency to barrel during the compression test.

The RTT-Non-aged samples were also prepared from solution annealed tubes of 316H steel which had been uniaxially strained as detailed in Table1.

2.2.2. Sample preparation

EBSD samples from the middle section of the tensile specimen's gauge length and from one third of the way along[2] from either end of the compression specimens were extracted from the deformed specimens by EDM and the mid-planes parallel and normal to the loading axis were studied. The surfaces were prepared by grinding sequentially with SiC papers followed by mechanical polishing with diamond paste down to a 1μm finish using a Struers Rotoforce automatic machine. The final preparation was electropolishing at 297K for 60s with Struers A21 electrolyte at 22V to remove all preparation-induced surface deformation.

2.2.3. EBSD orientation measurement

A field-emission gun scanning electron microscope (Zeiss Supra 55VP FEG SEM) fitted with NordlysF detector was used for automatic orientation mapping using a square grid pattern. The data acquisition and post processing was carried out using HKL fast acquisition-5.11 and Channel-5 software, respectively. The EBSD measurements were made using an accelerating voltage of 20 kV, a working distance of 15±0.1mm, a sample tilt of 70°, a step size of 1μm, a Hough resolution of 120 and an aperture size of 120μm in the high current mode.

As seen in Fig. 2 the deformation was very inhomogeneous. This inhomogeneity is characteristic of deformation of 316 steel but may have been exacerbated by the large variations in grain size in the ex-service steel apparent in Fig. 1& Fig. 2 as larger spreads of orientation after plastic deformation have been found in coarser grained than finer grained material in Cu, Ni and Fe [29].

Maps of the austenite orientation over an area 700μm x 700μm were obtained from all deformed samples with an indexing rate of above 97%. This large area measurement was to

[2] Finite element simulations indicate that in a compression test the strain at one third of the way along the axis is close to the overall measured strain.

accommodate deformation inhomogeneity as seen in Fig. 2 and only those maps with more than 100 grains were used for the strain analysis. No data cleaning was carried out, to avoid losing details associated with the plastic deformation. The 'noise' in the orientation measurement was determined by repeating the orientation mapping using identical conditions on a strain free germanium single crystal.

2.2.4. Hardness testing

An MTS Nano Indenter XP was used to measure the hardness of all deformed samples of the ex-service material on a surface prepared for EBSD measurement, using a maximum force of 49mN for 5s at a rate of 3.3mNs^{-1} and an indenter spacing of 18μm to prevent overlap of the indentation strain fields (the maximum indent size was ~ 6μm). Line-scan measurements were made over a total length of 700μm for each of the strained specimens to ensure sampling of multiple grains and the mean hardness was calculated based on the indenter's displacements from the surface at the maximum load.

2.2.5. Orientation data processing

The lattice orientations determined by EBSD were used to generate misorientation data quantified in terms of KAM, AMIS and LAMF.

2.2.5.1. KAM

The KAM metric was defined using a 3x3 kernel to assign an average misorientation to every measurement points in the orientation map using an equation of the form:

$$KAM(P) = \frac{1}{4}\sum_{e=1}^{4}[\theta(P,P_e]), For\ 0° \leq \theta \leq 2° \qquad (1)$$

where $\theta\ (P,\ P_e)$ is the misorientation between any point P and its neighboring points P_e as shown schematically in Fig. 3. This metric is a measure of local misorientation and represents the small lattice rotations between adjacent measurements points (local deformation) caused

by the accumulation of GNDs. To exclude misorientations associated with subgrain and grain boundaries, misorientations over 2° were disregarded in the calculation of KAM.

The KAM data from each deformed sample can be presented as a frequency distribution. The KAM distributions at different strains were compared with a variety of theoretical skewed probability distribution functions (PDFs) including Rayleigh, log-logistic, Weibull, lognormal and gamma distributions. The lowest statistical variances were given by gamma and lognormal PDFs which were then used to fit the frequency distributions of KAM over the whole analyzed area.

The gamma distribution models the sum of exponentially distributed random variables and is defined by:

$$f(x;k,\lambda)=\frac{1}{\lambda^k\Gamma(k)}x^{k-1}e^{\frac{x}{\lambda}}\quad \text{For } x \geq 0 \text{ and } k,\lambda > 0 \qquad (2)$$

where x is the variable (the KAM value in present case); k is the shape parameter; λ is the scale parameter and Γ is the gamma function [30]. The lognormal distribution takes the form:

$$f(x;\mu,\text{ø})=\frac{1}{x\text{ø}\sqrt{2\pi}}e^{\frac{-(\ln x-\mu)^2}{2\text{ø}^2}}\quad \text{For } x > 0 \qquad (3)$$

where μ and ø represent the logarithmic mean and the standard deviation of the distribution, respectively. For the lognormal distribution the mean is given by:

$$KAM_a = exp\left(\frac{\sum_{i=1}^{N}\ln x_i}{N}+\frac{\text{ø}^2}{2}\right) \qquad (4)$$

where, N is the total number of variables and for the gamma distribution the mean is given by $KAM_a = k\lambda$.

The closeness of the fit of the two theoretical PDFs to the experimental KAM data from samples with varied levels of plastic strain was assessed using both the regression variance and the significance of fitness tests. The mean of the fitted PDFs (KAM_a) was used

to represent the deformation at a particular plastic strain in each of the deformed samples and was calculated only from misorientations > 0.15° to reduce the effects of orientation noise.

2.2.5.2. AMIS

The AMIS metric was computed by taking the arithmetic mean of all spatially uncorrelated misorientations within each grain (grains being defined as regions bounded by misorientations greater than 15°) using equations of the form:

$$AMIS_I = \frac{1}{n}\sum_{i=1}^{n} \text{þ}(P, P_i) \quad AMIS_a = \frac{1}{m}\sum_{j=1}^{m} I_j \qquad (5)$$

where, $AMIS_I$ is the average intragrain misorientation for grain I; þ (P, P_i) is the misorientation between a reference point P and point P_i in grain I containing n measurement points and $AMIS_a$ is the overall intragrain misorientation from an orientation map containing m grains as shown schematically in Fig. 3. The mean grain orientation was used to define the reference point and only grains with equivalent circle diameter > 10μm were included in the calculation.

The extent of deformation varies from grain to grain so giving different average intragrain misorientations in each grain. A criterion based on the AMIS of each grain was used to determine the proportion of relatively undeformed grains (PUG) in each of the orientation maps. The $AMIS_a$ of undeformed material, which in the present case was about 1.5°, was used as a reference value for recognizing relatively undeformed grains. The PUG of any region of interest was defined as the fraction of grains with AMIS < 1.5°.

2.2.5.3. LAMF

The LAMF metric was based on point to point misorientations as shown schematically in Fig. 3 and was computed using the following equation:

$$LAMF = \frac{N(\theta_{2-15})}{N(\theta_{>2})} \qquad (6)$$

where $N(\theta_{2\text{-}15})$ is the number of misorientations with angles between 2°-15° and $N(\theta_{>2})$ is

the total number of misorientations in the orientation map with angles > 2°. The experimental results showed that the evolution of low angle misorientations with the increase in plastic strain was well represented by including a misorientation range of 2°-15° (see section 3.5) and the angular resolution of an EBSD system which uses a Hough transform to detect lines in the patterns is less than 1° [31] , so with proper EBSD system optimization it is possible to determine all misorientations above 2° absolutely. For these reasons a misorientation of 2° was taken as the lower limit of a subgrain boundary while misorientations >15° were regarded as high angle boundaries [17, 22, 32-34] .

2.3. *Effects of step- size*

Calculation of both KAM_a and LAMF is based on spatially correlated misorientations so their numerical values depend on the step size (distance between adjacent EBSD measurement points) used. To exclude effects other than the change in step-size, this was investigated using maps from an unstrained sample reconstructed using different step-sizes. As shown in Fig. 4, LAMF and KAM_a both increase almost linearly with the step-size while $AMIS_a$ remains constant as its computation is based on spatially uncorrelated misorientations. The step-size was kept constant at 1μm throughout the study.

2.4. *EBSD measurement parameters*

The accuracy of orientation measurements using EBSD can be improved by optimizing the measurement settings [15, 16, 35]. For a perfect crystal the mean spread in orientation about each point in the grain (KAM_a) should theoretically be zero. Instrumental factors [35] limit the angular resolution of standard EBSD resulting in a mean orientation noise in strain free material of about 0.3°-0.7° [36] which gives a finite minimum value of KAM_a. The KAM_a values obtained at different settings for the zero-strained aged steel and germanium single crystal are summarized in Table 2. KAM_a reduces with increases in the number of bands detected (BD), the Hough resolution (HR), the number of frames averaged

(FA), the aperture size (AS), the accelerating voltage (AV) and as the camera binning (CB) is reduced. The conditions highlighted in Table 2 are the best compromise for high angular resolution (i.e. relatively low KAM_a), high indexing rate (IR) and low acquisition time (AT) per measurement point and were used in the present study. KAM_a values from an unstrained germanium single crystal and unstrained aged steel are very similar confirming that for the undeformed material KAM_a is mainly determined by the accuracy of the orientation measurement. The small differences in their KAM_a values can be attributed to differences in sample preparation, mechanical history and the number of crystals analyzed.

3. Results

3.1 Flow behavior

Fig. 5 shows the flow curves obtained in HTT, SARTT and RTT tests. The uniformity of flow behavior at each temperature and strain rate is demonstrated by the overlay of the curves indicating that the deformed samples are representative of the plastic strain at each condition. Flows curves at 823K are characterized by lower flow stress and serrations compared with the 297K curves. The strain hardening rates ($d\sigma/d\varepsilon$) calculated from the true stress (σ) vs. true strain (ε) curves at 0.05 strain are about 2140MPa and 2670MPa for the HTT and RTT deformations, respectively. The flow behavior was similar in compression with a strain hardening rate of about 2760MPa at a true strain of 0.05 at 297K.

Fig. 6 shows flow curves from samples deformed in tension at 823K to 0.098 true plastic strains at rates ranging from $3.5x10^{-3}s^{-1}$ to $4x10^{-7}s^{-1}$. The flow stress remains very similar as the strain rate is reduced from $3.5x10^{-3}s^{-1}$ to $4x10^{-6}s^{-1}$ whereas a large reduction is seen at $4x10^{-7}s^{-1}$. There are conspicuous serrations on the flow curves at the intermediate strain rate of $3x10^{-5}s^{-1}$ which are barely detectable at high ($3.5x10^{-3}s^{-1}$) and low ($4x10^{-7}s^{-1}$) strain rates. The calculated strain hardening rates at 0.05 true strain are about 2250MPa and 1580MPa for tensile deformation at $3.5x10^{-3}s^{-1}$ and $4x10^{-7}s^{-1}$, respectively.

3.2 Hardness tests

The mean hardness (measured at room temperature) as a function of true plastic strain measured in tests at different temperatures (297K and 823K), deformation modes (tensile and compression) and strain rates down to $10^{-5}s^{-1}$ is shown in Fig. 7. The mean hardness increases almost linearly with increasing plastic strain. At each strain level there is no significant difference in the mean hardnesses of samples deformed under different conditions of temperature or mode except for an outlying result from the RTC compression sample at 0.187 true strain. The error bars shown are based on the standard error of the mean hardness of 39 indentation measurements made on each of the deformed samples.

The mean hardness of tensile samples deformed to a true strain of 0.098 at 823K reduces as the strain rate is reduced as shown in Fig. 8.

3.3 Distribution of misorientations

Fig. 9 (a & b) show comparisons between the fit of the lognormal distribution and the gamma distributions to the KAM frequency distributions obtained from samples deformed in tension to true plastic strains of 0.102 and 0.223, respectively at 823K. The fitted distributions both overestimate the mean value of the true distribution at low strain and underestimate it at higher strain. The mean of the theoretical distribution approaches the sample mean as its data fit improves.

The precision of the data fitting was judged using both the statistical variance from the true KAM distributions and likelihood-ratio tests [37]. For KAM data fitted with gamma, Rayleigh and lognormal PDFs the variance increases almost linearly as the true plastic strain is raised from 0 to 0.223, as shown in Fig. 10. The gamma PDF fit has consistently lower variance from the experimental data at all strain levels. For true strain >0.1 the divergence in the variances is significant indicating a clearly better fit of the gamma distribution while the difference is not significant for true strain < 0.1. The significance of fit of the PDFs computed

from the likelihood-ratio tests identified the lognormal PDF as a significantly better fit to the KAM data from samples with < 0.1 true strain while the gamma PDF was more appropriate for true strain > 0.1. To obtain a single value to accurately represent the degree of plastic deformation, allowance was made for the variation of local misorientations distribution with the level of plastic strain in the material by calculating KAM_a for each orientation map, using the formula of the best fitting theoretical PDF.

The spread in the misorientation distribution increases with the increase in both plastic strain and strain rate as shown in Fig. 11.

The misorientation distributions for tensile samples deformed to a true strain of around 0.18 under different conditions are shown in Fig. 12.

3.4 Plastic strain assessment using KAM

The correlation between the KAM_a and true plastic strain produced at different temperatures, deformation modes and strain rates down to $10^{-5}s^{-1}$ is shown in Fig. 13. The line is fitted using a Rodbard function [38] which gave smaller values of residual variance and sum of squared errors and higher values of fit probability and coefficient of determination than a linear fit or a polynomial of either second or third degree. The error bars shown are ± the standard error of the mean KAM_a of 4 orientation maps from each of the deformed samples.

The KAM_a increases with strain and at a given strain level no significant difference is seen between the values obtained under different deformation conditions but the KAM_a of the finer-grained non-aged material is consistently higher than that of the coarser grained materials. The rate of increase in KAM_a with strain is slightly less for true strains above 0.1 and is dependent on the misorientation range considered during KAM computation as shown in Fig. 14. As shown in Fig. 13 the SARTT tested sample had a markedly lower KAM_a compared to the aged tested samples of equivalent strain while the HTC samples have

slightly higher KAM_a than the other aged samples at true strains > 0.1. KAM_a is independent of the loading direction as the values obtained from the mid-planes parallel (PL) and normal (NL) to the loading axis show no significant difference.

Fig. 15 shows the relationship between the EBSD metrics and the strain rate for tensile samples deformed to a true strain of 0.098 at 823K. The KAM_a varies little with strain rate above $10^{-6}s^{-1}$ but appears to decrease for strain rates below this. A reduction of the EBSD camera binning from 4x4 to 2x2 reduces the KAM_a while maintaining the same trend of variation with strain rate.

Comparing specimens deformed to a true strain of 0.098, the proportion of grains with average intragrain misorientation < 1.5° increases as the strain rate is reduced as shown in Fig. 16.

3.5 Plastic strain assessment using LAMF

Fig. 17 shows the variation of the LAMF as a function of the included misorientation range for both undeformed samples and those with 0.223 true strain. The error bars shown are ± the standard error of the mean LAMF of 4 orientation maps at each strain level.

The relationship between the LAMF and the true plastic strain obtained under different conditions of temperature, deformation mode and strain rate down to $10^{-5}s^{-1}$ is shown in Fig. 18. The error bars shown are ± the standard error of the mean LAMF of 4 orientation maps from each of the deformed samples. A Rodbard function, shown by the dotted line in Fig. 18, was found to give the best fit to the data. Above 0.03 strain the LAMF increases with the strain at a decreasing rate leading to saturation at true strains above 0.15-0.2. At any given strain level LAMFs from samples deformed under different conditions are similar. The LAMFs of RTT-non-aged samples and the SARTT samples are significantly less than those of aged samples of equivalent strains. The LAMF is insensitive to the loading

direction as the values obtained from the mid-planes parallel and normal to the stress axis show no significant difference.

The relationship between the LAMF and the strain rate for samples deformed in tension to 0.098 true strain at 823K is shown in Fig. 15. From the 2x2 camera binned data LAMF appears to change little with strain rate but the 4x4 binned data suggests a monotonic decrease with the strain rate.

3.6 Plastic strain assessment using AMIS

The relationship between the $AMIS_a$ and true plastic strain under different conditions of temperature and deformation mode for strain rates down to $10^{-5}s^{-1}$ is shown in Fig. 19. The error bars shown are ± the standard error of the mean $AMIS_a$ of 4 orientation maps from each of the deformed samples and the line is fitted by linear regression. The $AMIS_a$ increases linearly with plastic strain although there is more scatter in the data for strains beyond 0.1. At each strain level the variations in $AMIS_a$ obtained under different deformation conditions are not significant although the values from the HTC samples appear slightly higher for true strains above 0.1. The $AMIS_a$ of RTT-non-aged and SARTT samples are lower than those of aged samples of equivalent strains again showing the influence of precipitation during thermal aging on the dislocation behavior but the effect on this metric is less than that on LAMF. Measurements carried out on mid-planes parallel and normal to the loading axis gave similar $AMIS_a$ values.

Fig. 15 shows $AMIS_a$ as a function of strain rate for samples deformed in tension to 0.098 true strain at 823K. The $AMIS_a$ reduces monotonically with strain rate. The reduction of EBSD camera binning from 4x4 to 2x2 increases the measured $AMIS_a$ but still shows the same trend of variation with the strain rate.

The variation of PUG with plastic strain under different deformation conditions is shown in Fig. 20. PUG decreases monotonically with strain and for strain rate down to $10^{-5}s^{-1}$

it appears insensitive to deformation temperature, mode, orientation of the measurement plane and thermal aging effects. However, PUG increases with decreasing strain rate as shown in Fig. 16. It appears that PUG might be applied generally to determine the strain experienced by austenitic steels regardless of their thermal histories.

3.7 EBSD metrics and hardness measurement

The hardness profile along the gauge length of a sample deformed in compression at 823K to 0.231 true strain is shown in Fig. 21. Barreling of the compressive specimens was more prevalent at 823K than at 297K, especially for true strains >0.15 which may have contributed to scatter in the values of KAM_a, LAMF and AMIS for the HTC specimens.

The results in Fig. 21 are the mean hardnesses from 39 indents at each measurement zone indicated. The mean hardness is highest around the middle of the specimen and reduces towards the ends. The measured barreling coefficient at this strain level was about 1.1.

Fig. 7 shows the relationship between the square root of $AMIS_a$ and the mean hardness of RTT and HTT deformed samples. The mean hardness increases monotonically with the square root of $AMIS_a$ regardless of the deformation temperature.

4. Discussion

4.1 Flow behavior

As shown in Fig. 5 & Fig. 6 the deformation behavior of the different samples is consistent and reproducible. The flow behaviors at 297K and 823K differ primarily in the values of the flow stress and the presence of serrations but also in the rate of the strain hardening, as previously observed [39]. Strain hardening is associated with changes in the dislocation density (ρ) which can be related to the flow stress using Taylor's equation $\sigma = \sigma_i + \alpha\mu b\rho^{0.5}$ (where σ_i is the overall crystal lattice resistance to dislocation movement, α is interaction constant, μ is the shear modulus, and b is the Burger vector) so these different flow stresses and strain hardening rates suggest that similar strain levels produced by

deformation at different temperatures may be associated with different dislocation densities and therefore different degrees of lattice orientation changes.

When at 823K the strain rate is decreased from $3.3x10^{-3}s^{-1}$ to $3x10^{-5}s^{-1}$ (see Fig. 6) the flow stress increases and serrations appear on the flow curve characterized by a pattern spikes with smaller variations in between during which period the strain hardening rate is lower than that overall. A further decrease in strain rate to $4x10^{-6}s^{-1}$ has a marginal effect on the flow stress but almost eliminates the serrations. 823K is known to be within the dynamic strain aging (DSA) regime for austenitic stainless steel deformed at about $10^{-4}s^{-1}$[40, 41] and the effects seen here result from DSA. Dislocation motion is interrupted by segregation of substitutional solute atoms (e.g. Cr) resulting in repeated yielding as the dislocations are unlocked from their solute atmospheres. Similar serrations in AISI 316 steel have been observed by [3, 41-43].The serrations seen here at $3x10^{-5}s^{-1}$ are typical of those seen at the high strain part of the DSA regime arising from the repeated unlocking and passage of deformation bands while at lower strain rates DSA of dislocations moving within the bands [44, 45] produces smaller more regular serrations.

Reducing the strain rate to $4x10^{-7}s^{-1}$ gives a smoother flow curve with a markedly reduced work hardening rate because at very low strain rates dislocations have more chance of climbing past obstacles.

4.2 Distribution of misorientations

Fig. 9 and Fig. 10 show that after deformation at 823K the local misorientation distributions from 316 steel strained to < 0.1 were closer to lognormal while for strains > 0.1 they were better fitted by a gamma distribution (although the variances from both distributions increased with the applied strain). A log-normal distribution arises from a random variable which can have only positive values. At low strains where dislocation densities are low and local misorientation values may be assumed to have a random

occurrence the distribution will be close to lognormal and be strongly skewed towards zero as seen in Fig. 11(a) . As strain and dislocation density increase more misorientations arise and both the mean and the spread of the distribution increase while the skew decreases. If the distribution of local misorientations remained random with increasing strain the distribution would be expected to approach a normal distribution for highly strained coarse-grained material so the variance from the lognormal distribution can be used as a rough measure of the dislocation content of a deformed structure. As seen in Fig. 10 the variance from this PDF increases with plastic strain. A lognormal distribution has been used [46, 47] to fit the distribution of misorientations from the grains' central orientations at strains > 0.1 in room temperature deformed 304 steel but those distributions show a much better fit to the lognormal at 0 strain than at a strain of 0.14. KAM is sensitive to very local changes in orientations and the change towards the gamma distribution with increasing strain found in the present work may reflect both the increased contributions from multiple slip and the greater interaction between dislocations as their density increases and they tend more and more towards a diffuse cellular arrangement. Direct observations by TEM of the dislocation structure of 316 steel deformed at room and intermediate temperatures (0.3-0.5 T_m) [46, 47] have shown that at lower strains dislocations are fairly homogeneously distributed in the grains and at grain boundaries (at the lowest strains at room temperature they are concentrated at the grain boundaries) but as the strain increases, dislocations in the grains are arranged in diffuse cell walls.

TEM measurements of misorientation angle distributions in deformed metals [48-50] have been exclusively on materials which form a well developed subgrain deformation structure and the distributions have been determined on the basis of the number of boundaries of a particular misorientation irrespective of their area rather than the result of sampling the misorientation distribution between points uniformly distributed in space as in EBSD but

[48, 49], when attempting to fit the distributions to a Rayleigh distribution ,noted a difference between the shape of the distributions (scaled by the mean misorientation) in Al cold rolled to 5% or 10% reduction compared to when it was deformed by 30% or 50% .

Although on the basis of TEM studies [50] concluded that the distribution of misorientations is independent of strain level, careful examination of the compilation of data from Al and Ni tested at room temperature, and 304 steel tested at 1273K show that the measured misorientation distributions are not exactly the same at different strain levels appearing more skewed at lower strains than at higher strains. Although the local dislocation arrangements differ in subgrain boundaries and diffuse cell walls and their energies and behavior will be different they are equivalent in terms of GNDs and so indistinguishable by EBSD.

As seen in Fig. 10 in the present case, the variances of the Rayleigh, lognormal and gamma distributions from that of the local misorientations were similar at low strains but at plastic strains above 0.1 the gamma distribution gave a much better fit.

The relationship between local misorientations and the extent of deformation is very complex. Although in polycrystals five independent active slip systems are necessary to accommodate the macroscopic shape changes of general plastic deformation, local regions within grains frequently deform by fewer slip systems and misorientations arise from different slip systems operating in neighboring regions of a crystal or from differences in activity on the same slip system [51]. Most work has been on materials with medium to high stacking fault energies so is difficult to apply to 316 steels. There have attempts to model the distributions of misorientations expected from arrival and absorption of up to three sets of dislocations at subgrain walls and compare the predictions with a Rayleigh distribution fit to the TEM observations [52] and later a model in which statistical fluctuations in dislocation fluxes cause accumulation of misorientations at subgrain boundaries [49] but this model

relies on many assumptions and is not affected by grain size so cannot be used to distinguish between different deformation mechanisms.

The increasing tendency to a gamma distribution for strains above 0.1 may result from sampling the misorientations from a dislocation structure increasingly organized into diffuse cells of rather larger size than the separation of the measurement points. This might be investigated by higher resolution mapping, at step sizes much smaller than those useful for plastic strain determination or by electron channeling contrast imaging.

TEM measurements of misorientation have a higher angular resolution than EBSD so reliably detect misorientations < 0.1° but sample only a very small volume, making it difficult to get representative results when, as seen in Fig. 2 deformation is frequently highly inhomogeneous. The strength of EBSD in studying deformation is its ability to sample much larger volumes.

The evolution of the distributions of lattice misorientations in aged 316 steel with imposed plastic strain at 823K (Fig. 11 (b)) shows a progressive change with strain rates of $10^{-3}s^{-1}$, $10^{-5}s^{-1}$ and $10^{-7}s^{-1}$ with the misorientation distribution sharpening towards lower misorientations as the strain rate is reduced but the result for $10^{-6}s^{-1}$ seems anomalous. There are two possible explanations for the overall change; firstly that dynamic recovery takes place so that dislocations rearrange to lower energy configurations and the misorientation distribution sharpens or secondly that at lower strain rates thermally activated deformation mechanisms other than dislocation generation and accumulation in the body of the grain contribute to the overall strain. In the latter case the reduced dislocation density would account for the observed reduction in both the mean and the spread of the distribution at lower strain rates. Since the flow curves show that DSA occurs at 823K solute interactions with dislocations may also be affecting the build up of the misorientation distribution, which

could, depending on the time constants for diffusion of the solute concerned, account for the anomalous behavior around $10^{-6}s^{-1}$.

Comparison of the misorientation distributions for tensile samples deformed to around 0.18 true strain under different conditions (Fig. 12) allows distinction between the effects of test temperature, grain size and precipitation or other thermal aging effects. The RTT and HTT samples show very similar behavior with a slight reduction in both the mean and the spread of the distributions from the HTT as compared to the RTT. This is consistent with similar deformation behavior at the two temperatures at these moderate strain rates. The slight reductions in the mean and spread show a small contribution from thermally activated processes during the HTT deformation. The re-solution-annealed aged material (SARTT) which had no precipitates and a similar but slightly larger grain size than the aged material had a lower mean misorientation and a slightly narrower misorientation distribution than the RTT but the RTT-non-aged material which had a smaller grain size and no precipitates had both a higher mean misorientation and a broader spread of misorientations. This shows that EBSD captures the effect that both reducing the grain size and aging cause an increase in the rate of dislocation accumulation with increasing strain and so independently contribute to hardening.

4.3 Plastic strain characterization using KAM

As shown in Fig. 13 the relationship between KAM_a and known plastic strain is independent of deformation temperature and mode for strain rates down to ~$10^{-5}s^{-1}$. This suggests a similar evolution of the lattice misorientations with strain at 823K to that at 297K despite the much lower flow stresses (Fig. 5). TEM studies [53] showed a much more rapid increase in overall dislocation density both at the grain boundaries and in the body of the grains of 316L steel deformed at 293K rather than 673K. Here the similarity of KAM_a after deformation to the same strain at the two different temperatures despite the difference in flow

stresses suggests that locally the GND densities are similar even though the overall dislocation densities may be different. At 823K DSA affects the flow stress and at this intermediate temperature it is also possible that some grain boundary sliding occurred [54]. If grain boundary sliding occurs the dislocations accommodating this will be localized close to the boundary and due to their proximity to this grain boundary the misorientations they produce would be excluded from the calculation of KAM. KAM_a is little affected by the orientation of the measurement plane, suggesting that the spatial distribution of misorientations is independent of the loading direction for true strains up to 0.223. The strain sensitivity of KAM_a reduces slightly for plastic strains > 0.1 as shown in Fig. 13 by diminishing increments in KAM_a with increasing strain. The density of GNDs has been shown to increase linearly with strain [55] so this saturation in KAM_a is due to the nature of the metric rather than changes in dislocation behavior. KAM_a is calculated considering only misorientations of 0.15°-2° so its value saturates at high strains as more of the local misorientations approach the upper limit. Therefore, the nature of the correlation in Fig. 13 depends on the metric's definition, as shown in Fig. 14: reducing the included misorientation range makes KAM_a saturate at lower strains. These results demonstrate that the relationship between bounded EBSD metrics such as KAM_a and true plastic strain is not always linear at the extremes of the strain range. The saturation tendency introduces an asymptotic region in the graph of KAM_a against true plastic strain (ε) and the data can be fitted by a Rodbard function described by:

$$KAM_a = d + \frac{(a-d)}{\left[1+\left(\frac{\varepsilon}{c}\right)^b\right]} \qquad (7)$$

where *a*, *b*, *c* and *d* are constants determined by the position of the upper asymptote, the slope of the linear region, the location of the transition region and the position of the lower

asymptote, respectively [56]. The relationship between KAM_a and strain derived from all the data from ex-service material in Fig. 13 is described by:

$$KAM_a = 3.314 - \frac{3.014}{\left[1 + \left(\frac{\varepsilon}{0.770}\right)^{1.178}\right]} \quad (8)$$

4.4 Plastic strain characterization using LAMF

Lattice misorientations resulting from GNDs such as arrays of dislocations accumulated at obstacles in the microstructure contribute to the low angle misorientation fraction. As shown in Fig. 17 using the misorientation range 2°-15° to define a 'low angle misorientation' gives a large change in LAMF for a given strain (ε) difference while reducing the effect of orientation noise. Fig. 18 shows that as the global plastic strain increases LAMF increases at a reducing rate. This is because at high strains high angle misorientation (>15°) develop which reduces LAMF. At low strains the metric's sensitivity is reduced by the orientation 'noise' and by the presence of real low angle boundaries in the microstructure which prevent the LAMF value falling to zero at 0 strain. Like KAM_a, the LAMF is insensitive both to deformation mode and the orientation of the measurement plane.

The relationship shown in Fig. 18 suggests that the variation of LAMF with applied plastic strain is most sensitive over the range 0.05-0.15 strain. The correlation between LAMF and strain can be fitted with a Rodbard function which for all the data from the aged material is given by:

$$LAMF = 0.938 - \frac{0.855}{\left[1 + \left(\frac{\varepsilon}{0.089}\right)^{2.818}\right]} \quad (9)$$

As seen in Fig. 15, reducing the camera binning, which improves the detection of low angle misorientations, increases the numerical value of LAMF.

4.5 Plastic strain characterization using AMIS

Whereas KAM is a very local measure of misorientation, AMIS is a measure of the longer range misorientations across the grain. Fig. 19 shows that $AMIS_a$ is higher in the aged material than in the non-aged material at the same strain. This cannot be attributed solely to the coarser grains in the aged material (100µm as opposed to 30µm grain size) [29] because solution annealed ex-service material shows a similar $AMIS_a$ to the non-aged steel. This shows that the presence of intergranular and intragranular precipitates assists the generation and accumulation of GNDs during deformation. The value of $AMIS_a$ is unaffected by the deformation mode or the loading direction.

In contrast to the bounded metrics KAM and LAMF, the whole range of possible misorientations is included in $AMIS_a$ and this metric increase monotonically with plastic strain. This result suggests a constant increase in the net crystal rotations resulting from the generation and storage of GNDs over the strain range 0-0.23 and strain rates down to $10^{-5}s^{-1}$ at temperatures 297K and 823K. As seen in Fig. 15, reducing the camera binning, which improves the EBSD angular resolution, increases the measured $AMIS_a$ because increasing the accuracy of each orientation measurement improves the detection of very low angle misorientations.

Fig. 19 indicates that the sensitivity of $AMIS_a$ in assessing plastic strain is good at all strain levels investigated. For the aged material the relationship can be fitted by a straight line of the form:

$$AMIS_\alpha = 24.02\varepsilon + 0.96 \qquad (10)$$

4.6 Proportion of Undeformed Grains

As seen in Fig. 20 the variation of PUG with the applied strain appears unaffected by thermal aging effects, deformation temperature, mode or orientation of the measurement plane. This metric may therefore be generally applicable for strain assessment in austenitic

stainless steels regardless of their thermal histories or grain sizes. Although the solution annealed material and the aged material had different grain sizes, neither of them showed strong texture. Further work is necessary to establish how PUG depends on texture but it seems to offer a very simple way to follow deformation. The relationship

$$PUG = 0.0142 + \frac{0.823}{\left[1 + \left(\frac{\varepsilon}{0.045}\right)^{2.329}\right]} \qquad (11)$$

has been derived from all the data in Fig. 20.

4.7 Effects of aging

The most obvious effect of long term aging during service is extensive precipitation, both intragranularly and at the grain boundaries. These precipitates not only harden the metal by creating additional obstacles to dislocation flow but their interfaces provide additional dislocation sources and sinks. As seen by comparing Fig. 2 (a & b) grain boundary precipitates also complicate the transfer of slip across grain boundaries and initiate complex slip earlier than clean grain boundaries. The RTT-non-aged material is finer grained so might be expected to have a lower value of LAMF (because there are more high angle grain boundaries per unit volume to start with) but Fig. 18 shows that at about 0.18 true strain LAMF is higher in the aged material than in either the solution annealed ex-service material or the non-aged material, so aging must cause this increase. Slip bands and dislocation pile ups at precipitates will tend to concentrate misorientation locally, giving more misorientations in the range 2°-15° between points 1µm apart in the aged than in the SA material and so increasing the measured LAMF.

The increase in AMIS caused by aging shows that precipitation assists the generation and accumulation of GNDs during deformation. It is possible that dislocation tangles around precipitates and the generally greater complexity of deformation in grains containing harder particles may make it easier for differences to arise in the activation of different slip systems

in local volumes of the grain and so might stabilize a smaller cell size in the deformation structure of the aged material than in the SA. As AMIS is a measure of the longer range misorientations across a grain, if the misorientation change at each diffuse cell boundary is similar this could explain the increased AMIS using a random walk argument.

KAM is a measure of the local misorientations and it is again higher in the aged material than in the SA material of a similar grain size reflecting the concentration of dislocation tangles around the precipitates in the aged material. It is interesting that although the LAMF and AMIS values of the SARTT are very similar at the same strain level, KAM is consistently higher in the non-aged material than in the re-solution annealed or aged but this is probably due to the finer grain size of the non-aged material used.

4.8 Strain rate dependence of deformation and its effect on EBSD measurements

As shown in Fig. 15, both LAMF and $AMIS_a$ decrease with reducing strain rate over the whole range studied. The effect on LAMF may result from the change in misorientation distributions seen in Fig. 11(b). As the strain rate reduces more and more misorientations will fall below its lower bound. As seen in Fig. 15 only at strain rates less than $4x10^{-6}s^{-1}$ is calculated KAM_a sensitive to the strain rate and there appears to be a rate sensitivity limit somewhere between $4x10^{-6}s^{-1}$ and $4x10^{-7}s^{-1}$. This difference in behavior is probably linked to the difference in the angular ranges of misorientations considered by the metrics; KAM disregards any misorientation > 2°, LAMF is calculated only from those between 2°-15°, while AMIS considers all misorientations in a given grain. This will make KAM less sensitive to GNDs forming subgrain walls than the other metrics. Any increased tendency to grain boundary sliding at $\sim10^{-7}s^{-1}$ would also result in a reduced dislocation content away from the immediate vicinity of the grain boundaries and thus a lower KAM_a.

As seen in Fig. 16 the proportion of relatively undeformed grains increases as the strain rate decreases which again suggests that at lower strain rates deformation mechanisms

other than dislocation generation and movement within the grains contribute more to the total deformation . The strain rate dependence of the mean hardness (Fig. 8) also corresponds well with that of the EBSD metrics and shows clearly that the strain rate has a significant effect on the deformation. The mean hardness (H_{nano}) varies as the square root of $AMIS_a$ (Fig. 7) with the correlation described empirically as:

$$H_{nano} = 1.08\sqrt{AMIS_a} + 1.32 \qquad (12)$$

This suggests a close relationship between the $AMIS_a$ and the dislocation density which is related to the material's hardness by $HV_n = \alpha\mu b\rho^{0.5}$ where HV_n is the Vickers hardness of the material [57]. However, the value of $AMIS_a$ is affected only by the GNDs which are responsible for the lattice orientation changes and not by the statistically stored dislocations (SSDs) which have zero net Burgers vector while the hardness is expected to depend on the total dislocation content.

All these changes indicate that as the strain rate is reduced the number of GNDs at any particular strain level reduces. This must either be due to fewer being generated or more being annihilated. If a mechanism such as grain boundary sliding, which is accommodated in a region close to the boundary, contributes to deformation this need not generate an excess of dislocations of a particular sign in the grain interiors. Observations of grain shape changes during deformation[54] have indicated that grain-boundary sliding can contribute significantly to deformation of 316L stainless steel at intermediate temperatures and low strain rates. The number of low angle grain boundaries has been observed to reduce with strain rate in precipitation hardened aluminum-copper alloys [58] but this was caused by dynamic grain growth. The Ashby deformation map [59] indicates that 823K is too low a homologous temperature (0.45 T_m) for dynamic recovery but Fig. 11 (b) suggests that at low strain rates it may occur. It is also possible that at these temperatures Coble creep may make a small contribution to the total deformation. At lower strain rates it is possible that thermally

activated processes such as unpinning or climb of favorably oriented SSDs which then become mobile may make a greater contribution to the total deformation (and so reduce the number of GNDs that needed to be generated) than at higher strain rates. Alternatively thermally activated unpinning or climb of otherwise immobile GNDs may allow them to glide to sinks such as grain boundaries or precipitate-matrix interfaces or to annihilate with others of opposite sign.

The consistent indications of an effect of strain rate on the misorientations produced during plastic deformation to a particular strain found in this study are in contrast to previous comparisons on a 2.25%Cr-1%Mo steel between tensile and creep deformations at 873K [24] which found no significant difference. However the metric used in that case considered only a very limited number of measurement points in each grain which could have reduced its sensitivity to orientation changes, especially for the creep deformation which is heterogeneous [60]. The dependence of the lattice misorientations developed during deformation on the strain rate shows that EBSD can be used to discern transitions between deformation mechanisms.

4.9 Correlation between the results obtained by EBSD and by hardness measurement

EBSD and nanoindentation have very different spatial resolutions and the extents of the strain fields they analyze differ by orders of magnitude. The lateral spatial resolutions were 1μm and 18μm for the EBSD and nanohardness measurements respectively, while the depth sampled by the hardness measurement was about 1μm and by the EBSD technique 10-100nm [11, 12] . However, as shown in Fig. 7, the EBSD metrics and the mean hardness are similar in their responses to differences in deformation conditions in terms of strain, temperature, mode and strain rates. This is shown particularly in the similar strain rate dependence of both hardness and AMIS (see Fig. 8 and Fig. 15).

Fig. 7 shows that at similar strain rates the mean hardness increases linearly with the plastic strain and at strain rates around $10^{-4}s^{-1}$ to $10^{-5}s^{-1}$ can be expressed empirically as:

$$H_{nano} = 6.5\varepsilon + 2.6 \quad (13)$$

This suggests that, despite the additional hardening caused by precipitation during service, hardness surveys could still be used for long term monitoring of plastic strain in 316 steel power plant components. However, the subtle differences in the straining hardening at the two temperatures (seen in the flow curves) cannot be distinguished by the hardness measurement which appears insensitive to deformation temperature. The scatter in the hardness data can be attributed to local microstructural variations such as in precipitate density or local grain sizes (Fig. 1) and to the inhomogeneity of deformation as seen in Fig. 2.

4.10 Application to measuring strain around a weld

The empirical equations presented in this paper (Eqns. 8-13) derived for an aged 316 steel can be applied for quantifying the degree of plastic strain in power plant components made of similar material. Fig. 22 shows the plastic strain distribution around a weld in an ex-service 316 stainless steel steam header derived from EBSD measurements and calculated using the relationship between $AMIS_a$ and plastic strain for aged 316 steel (Eqn. 10)

For comparison the strain distribution calculated using the data for solution annealed 316 steel are also included. The use of data from the SA material leads to a significant over-estimation of the strain around the weld which might in turn indicate a greater susceptibility to stress corrosion cracking and shorter remaining lifetime than the true values and might lead to unnecessarily early decommissioning.

5. Conclusions

The evolution of lattice misorientations in an aged AISI 316H austenitic stainless steel as a function of plastic strain reached under different deformation conditions of temperature, mode and strain rate has been quantified using EBSD. The applicability of the

EBSD metrics KAM_a, LAMF , $AMIS_a$ and PUG in assessing plastic strain under different deformation conditions has been demonstrated and the results validated by nanohardness measurement. Characterization of the misorientation evolution with increasing plastic strain has provided insights on the behavior of the EBSD metrics and on the nature of the deformation under different conditions. The main conclusions drawn are:

- The distribution of local misorientations depends on the imposed plastic strain being best described by a lognormal distribution at true strains < 0.1 and by a gamma distribution at strains > 0.1. This is attributed to the increasing effects of dislocation-dislocation interactions as the strain increases.
- Different deformation conditions of strain, temperature, strain rate and mode have very similar effects on the measured hardness and the EBSD metrics. The measured hardness varies as the square root of the $AMIS_a$ value suggesting a good correspondence between the $AMIS_a$ and the dislocation density.
- The development of lattice misorientations during tensile deformation to a true strain of 0.098 at 823K depends on the applied strain rate. The distribution sharpens towards low misorientations values as strain rate is reduced. This suggests a change in the deformation mechanism which gives rise to reduced dislocation densities as the strain rate is reduced.
- During high temperature plastic deformation the local misorientation distribution varies with the strain rate demonstrating the potential of EBSD in identifying changes in the deformation mechanisms in austenitic stainless steels. Calibration curves derived from room temperature tests should therefore not be used for estimating strain developed at high temperatures when strain rates are less than $10^{-5}s^{-1}$.
- LAMF and $AMIS_a$ decrease monotonically with decreasing strain rate while KAM_a appears to have a rate sensitivity limit between $4x10^{-6}s^{-1}$ and $4x10^{-7}s^{-1}$ above which it is

insensitive to strain rate. PUG on the other hand increases with a reduction in strain rate.

- Empirical relationships have been derived between the EBSD metrics and the applied plastic strain of long-term aged 316 steel which can be used for estimating the strain experienced by similar materials e.g. around welds.
- The strain sensitivity of the different EBSD metrics is related to the misorientation ranges considered in their calculation. KAM_a and PUG are best used for true strains 0-0.15, LAMF for true strains 0.05-0.15 while $AMIS_a$ is good at all strain levels considered. All metrics apart from PUG depend on the material's thermal history demonstrating the influence of microstructure on the evolution of misorientations during deformation. The variation of PUG with applied strain was independent of thermal history and grain size showing its potential for strain assessment in austenitic stainless steels.

6. Acknowledgements

The authors wish to acknowledge EDF Energy for partly funding the project and for providing the material used in the study.

7. References

1. P. Marshall: *Austenitic Stainless Steels: Microstructure and Mechanical Properties,* Elsevier Applied Science, Essex, 1984, pp. 80-102, 185.
2. J.R. Davis: *ASM Speciality Handbook: Stainless Steel,* ASM International, Ohio, 1994, pp. 20-32.
3. D. Fahr: *Analysis of stress-strain behavior of type 316 stainless steel,* OAK Ridge National Laboratory, Tennessee, 1973, pp. 1-22.
4. P.L. Andresen, and M.M. Morra: *J. Nucl. Mater.,* 2008, vol. 383, pp. 97-111.
5. J. Hou, Q.J. Peng, T. Shoji, J.Q. Wang, E.H. Han, and W. Ke: *Corros. Sci.,* 2011, vol. 53, pp. 2956-62.
6. A. Turnbull, K. Mingard, J.D. Lord, B. Roebuck, D.R. Tice, K.J. Mottershead, N.D. Fairweather, and A.K. Bradbury: *Corros. Sci.,* 2011, vol. 53, pp. 3398-415.
7. M. Kamaya: *Mater. Charact.,* 2009, vol. 60, pp. 125-32.

8. P.J. Buchanan, V. Randle, and P.E.J. Flewitt: *Scr. Mater.,* 1997, vol. 37, pp. 1511-18.
9. K. Masayuki: *Ultramicroscopy,* 2011, vol. 111, pp. 1189-99.
10. R. Yoda, T. Yokomaku, and N. Tsuji: *Mater. Charact.,* 2010, vol. 61, pp. 913-22.
11. K.Z. Baba-Kishi: *J. Mater. Sci.,* 2002, vol. 37, pp. 1715-46.
12. R.A. Schwarzer, D.P. Field, B.L. Adams, M. Kumar, and A.J. Schwartz: Present state of electron backscatter diffraction and prospective developments, in: A.J. Schwartz, M. Kumar, and B.L. Adams (Eds.): *Electron Backscatter Diffraction in Materials Science* Kluwer Academic/Plenum Publishers, London, 2009, pp. 1-19.
13. A. Arsenlis, and D.M. Parks: *Acta Mater.,* 1999, vol. 47, pp. 1597-611.
14. A.J. Wilkinson, and D.J. Dingley: *Acta Metall. Mater.,* 1991, vol. 39, pp. 3047-55.
15. T. Maitland, and S. Sitzman: Electron backscatter diffraction (EBSD) technique and materials characterization examples, in: W. Zhou, and Z.L. Wang (Eds.): *Scanning Microscopy for Nanotechnology: Techniques and Applications,* Springer Science, New York, 2007, pp. 41-75.
16. F.J. Humphreys: *J. Mater. Sci.,* 2001, vol. 36, pp. 3833-54.
17. S.I. Wright, M.M. Nowell, and D.P. Field: *Microsc. Microanal.,* 2011, vol. 17, pp. 316-29.
18. M. Kamaya, A.J. Wilkinson, and J.M. Titchmarsh: *Acta Mater.,* 2006, vol. 54, pp. 539-48.
19. M. Kamaya, A.J. Wilkinson, and J.M. Titchmarsh: *Nucl. Eng. Des.,* 2005, vol. 235, pp. 713-25.
20. A. Sáez-Maderuelo, L. Castro, and G. Diego: *J. Nucl. Mater.,* 2011, vol. 416, pp. 75-79.
21. J.J. Sanchez-Hanton, and R.C. Thomson: *Mater. Sci. Eng. A,* 2007, vol. 460-461, pp. 261-67.
22. E.M. Lehockey, L. Y.;, and O.E. Lepik: Mapping residual plastic strain in materials using electron backscatter diffraction, in: A.J. Schwartz, M. Kumar, and B.L. Adams (Eds.): *Electron Backscatter Diffraction in Materials Science,* Kluwer Academic, New York, 2000, pp. 247-60.
23. J. Kang, B. Bacroix, H. Regle, K. Oh, and H. Lee: *Acta Materialia,* 2007, vol. 55, pp. 4935-46.
24. C. Fukuoka, K. Morishima, H. Yoshizawa, and K. Mino: *Scr. Mater.,* 2002, vol. 46, pp. 61-66.
25. R. M'Saoubi, and L. Ryde: *Mater. Sci. Eng. A,* 2005, vol. 405, pp. 339-49.
26. K. Fujiyama, K. Mori, D. Kaneko, H. Kimachi, T. Saito, R. Ishii, and T. Hino: *Int. J. Pressure Vessels Piping,* 2009, vol. 86, pp. 570-77.
27. D.J. Child, G.D. West, and R.C. Thomson: *Acta Mater.,* 2011, vol. 59, pp. 4825-34.
28. D.P. Field, K.R. Magid, I.N. Mastorakos, J.N. Florando, D.H. Lassila, and J.W. Morris: *Philos. Mag.,* 2010, vol. 90, pp. 1451-64.
29. S. Scheriau, and R. Pippan: *Mater. Sci. Eng. A,* 2008, vol. 493, pp. 48-52.
30. A.J. Hayter: *Probability and Statistics for Engineers and Scientists,* Brooks/Cole Centage Learning, Boston, 2012, pp. 199-202.
31. S. Zaefferer: *Cryst. Res. Technol.,* 2011, vol. 46, pp. 607-28.
32. D. Dingley: *J. Microsc.,* 2004, vol. 213, pp. 214-24.
33. O.V. Mishin, A. Godfrey, and D.J. Jensen: Analysis of deformation structures in FCC materials using EBSD and TEM techniques, in: A.J. Schwartz, M. Kumar, and B.L. Adams (Eds.): *Electron Backscatter Diffraction in Materials Science,* Springer Science, New York, 2009, pp. 263-75.
34. H. Mirzadeh, J.M. Cabrera, A. Najafizadeh, and P.R. Calvillo: *Mater. Sci. Eng. A,* 2012, vol. 538, pp. 236-45.

35. F.J. Humphreys, Y. Huang, I. Brough, and C. Harris: *J. Microsc.,* 1999, vol. 195, pp. 212-16.
36. I. Brough, P.S. Bate, and F.J. Humphreys*,* 2006, vol. 22, pp. 1286-86.
37. A. Agresti: *An Introduction to Categorical Data Analysis,* John Wiley & Sons, Inc., New Jersey, 2007, pp. 35-36;.
38. Z. Govindarajulu: *Statistical Techniques in Bioassay,* S. Karger AG, Basel, 2001, pp. 197-199.
39. T.S. Byun, N. Hashimoto, and K. Farrell: *Acta Mater.,* 2004, vol. 52, pp. 3889-99.
40. S. Venugopal, S.L. Mannan, and Y.V.R.K. Prasad: *J. Nucl. Mater.,* 1995, vol. 227, pp. 1-10.
41. K.G. Samuel, S.L. Mannan, and P. Rodriguez: *Acta Metall.,* 1988, vol. 36, pp. 2323-27.
42. E.I. Samuel, B.K. Choudhary, and K.B.S. Rao: *Scr. Mater.,* 2002, vol. 46, pp. 507-12.
43. C.G. Shastry, M.D. Mathew, K.B.S. Rao, and S.D. Pathak: *Mater. Sci. Technol.,* 2007, vol. 23, pp. 1215-22.
44. P. Rodriguez: *Bull. Mater. Sci.,* 1984, vol. 6, pp. 653-63.
45. M.T. Nogueira, and M.A. Fortes: *Scr. Metall.,* 1984, vol. 18, pp. 505-08.
46. B.P. Kashyap, K. McTaggart, and K. Tangri: *Philos. Mag.,* 1988, vol. 57, pp. 97-114.
47. B.P. Kashyap, and K. Tangri: *Acta Metall. Mater.,* 1995, vol. 43, pp. 3971-81.
48. D.A. Hughes, Q. Liu, D.C. Chrzan, and N. Hansen: *Acta Mater.,* 1997, vol. 45, pp. 105-12.
49. W. Pantleon: *J. Mater. Res.,* 2002, vol. 17, pp. 2433-41.
50. D.A. Hughes, D.C. Chrzan, Q. Liu, and N. Hansen: *Phys. Rev. Lett.,* 1998, vol. 81, pp. 4664-67.
51. B. Bay, N. Hansen, D.A. Hughes, and D. Kuhlmann-Wilsdorf: *Acta Metall. Mater.,* 1992, vol. 40, pp. 205-19.
52. W. Pantleon, and N. Hansen: *Acta Mater.,* 2001, vol. 49, pp. 1479-93.
53. M. Janecek, and K. Tangri: *J. Mater. Sci.,* 1995, vol. 30, pp. 3820-26.
54. K.J. Kurzydlowski, K.J. McTaggart, and K. Tangri: *Philos. Mag.,* 1990, vol. 61, pp. 61-83.
55. C.C. Merriman, D.P. Field, and P. Trivedi: *Acta Mater.,* 2008, vol. 1, pp. 153-62.
56. P.G. Gottschalk, and J.R. Dunn: *Anal. Biochem.,* 2005, vol. 343, pp. 54-65.
57. M. Predeleanu, and P. Gilormini: *Advanced Methods in Materials Processing Defects,* Elsevier science B.V, Amsterdam, 1997, pp. 100-102.
58. O.V. Rofman, P.S. Bate, I. Brough, and F.J. Humphreys: *J. Microsc. ,* 2009, vol. 233, pp. 432-41.
59. H.J. Frost, and M.F. Ashby: *Deformation-Mechanism Maps: The Plasticity and Creep of Metals and Ceramics,* Elsevier Science & Technology, London, 1982, pp. 60.
60. R.W. Evans, and B. Wilshire: *Introduction to Creep,* The Institute of Materials, London, 1993, pp. 38, 49.

8. List of Figures

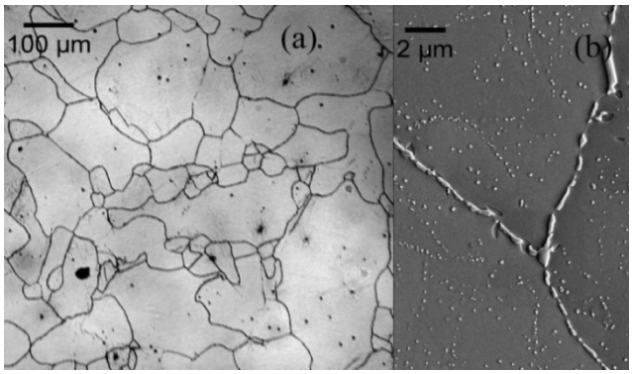

Fig. 1. (a) Optical micrograph of the aged AISI 316H austenitic stainless steel showing wide variations in grain sizes. (b) SEM micrograph showing intergranular and intragranular precipitates.

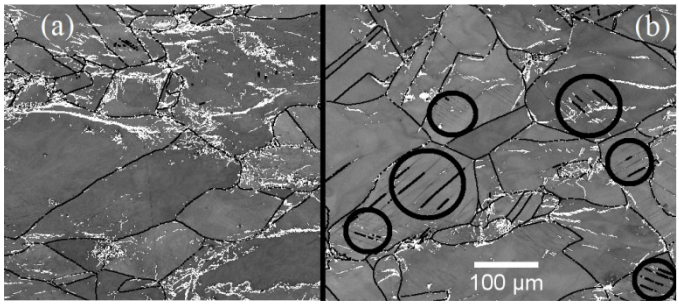

Fig. 2. Image quality map superimposed with low angle misorientation map showing deformation inhomogeneity for (a) the aged steel deformed to 0.187 true strain at 297K. Deformed zones are represented by 'white patches' and grain boundary by misorientations > 15° (continuous black line). (b) Solution annealed steel deformed to 0.187 at 297K showing slip bands (circled regions) in different grains.

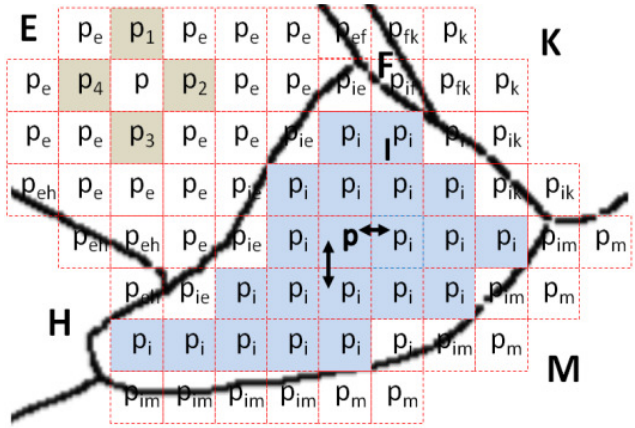

Fig. 3. Schematic illustration of an orientation map with EBSD measurement points on a square grid. Thick black lines show misorientations >15° separating grains E, F, H, I, K and M. Points considered for KAM and AMIS computations are shaded in grain E and I, respectively. The arrows on point P in grain I show the adjacent points considered in the determination of the LAMF.

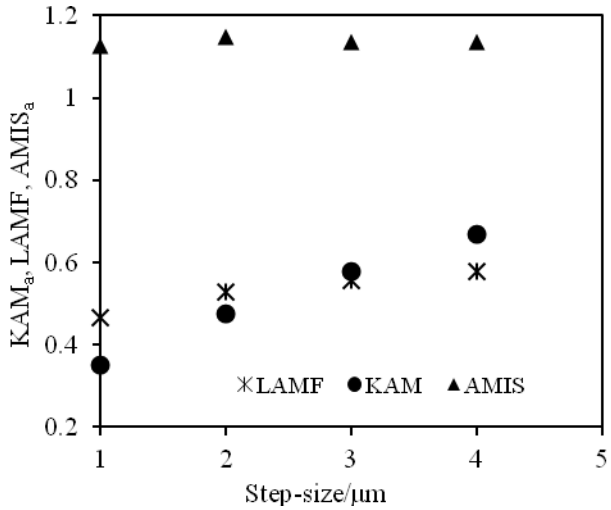

Fig. 4. The step-size dependence of the KAM_a, LAMF and $AMIS_a$ values from undeformed sample.

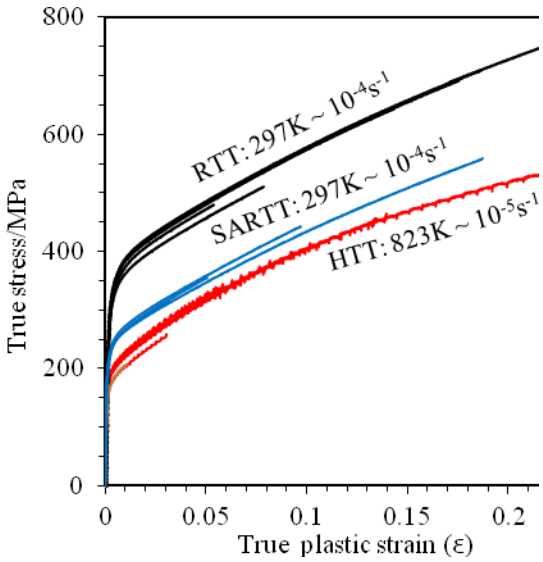

Fig. 5. Flow curves for the aged and solution annealed AISI Type 316H steel obtained at different temperatures and strain rates.

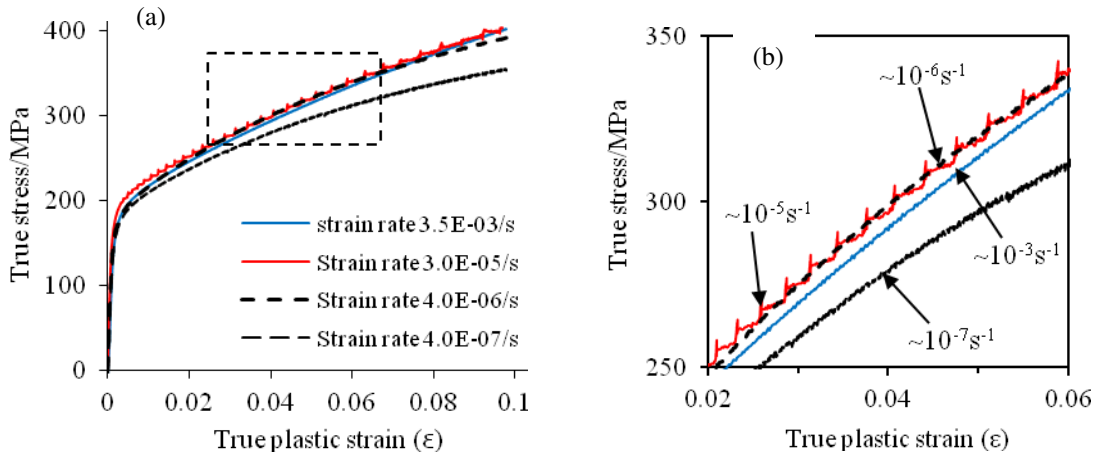

Fig. 6. (a) Strain rate dependence of the flow behavior of the aged steel deformed in tension to 0.098 true strain at 823K. (b) Magnification of the region marked by dashed rectangle.

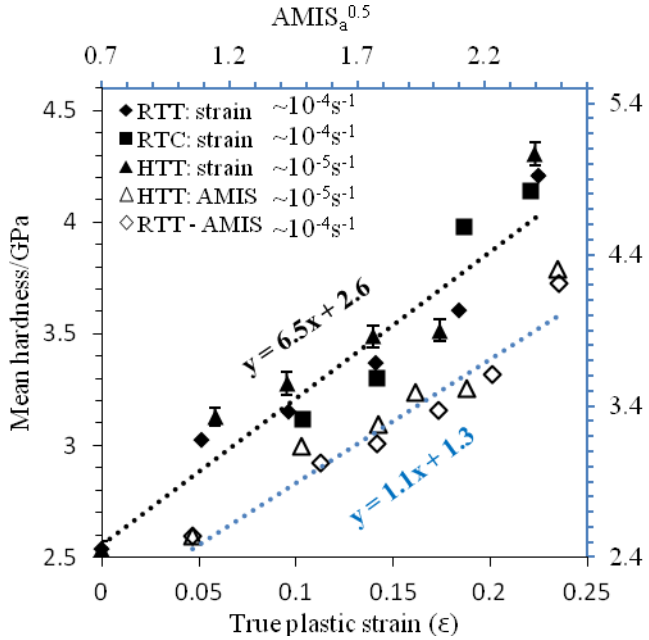

Fig. 7. Primary axis: mean hardness of RTT, RTC and HTT tested samples versus true plastic strain. Secondary axis: mean hardness values of HTT and RTT tested samples versus square root of $AMIS_a$ (Lines fitted by linear regression.)

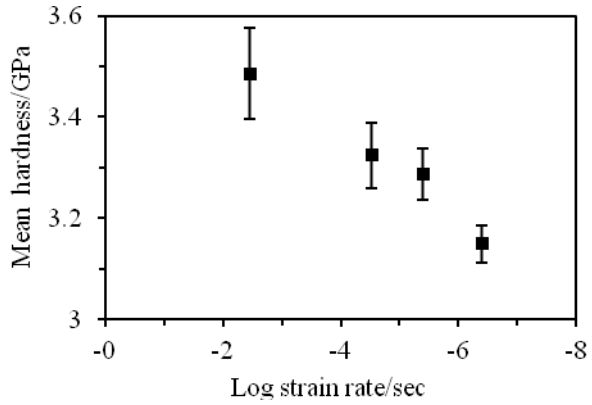

Fig. 8. Strain rate dependence of the mean hardness of the HTST tested samples.

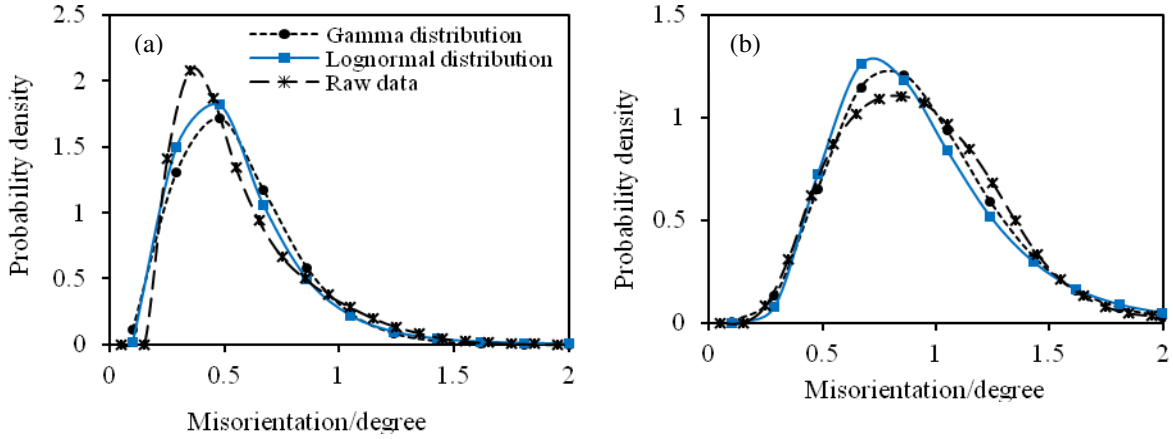

Fig. 9. Fitting of gamma and lognormal PDFs to the KAM frequency distribution obtained from samples deformed in tension to (a) 0.102 and (b) 0.223 true strains at 823K.

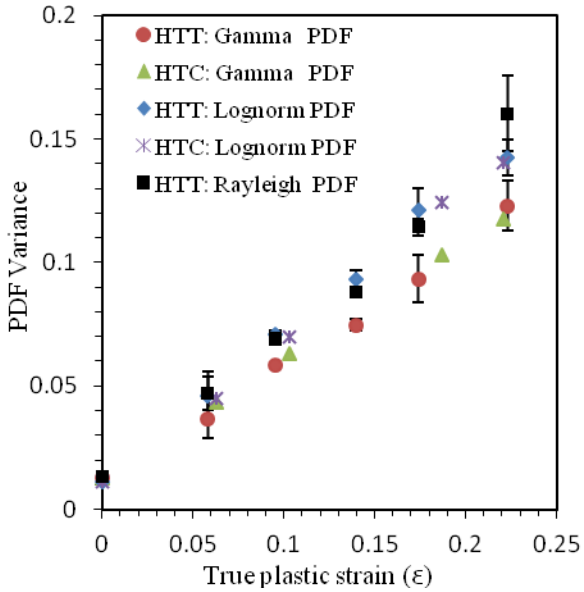

Fig. 10. Statistical variance versus true plastic strain at 823K for KAM data fitted with gamma, Rayleigh and lognormal PDFs.

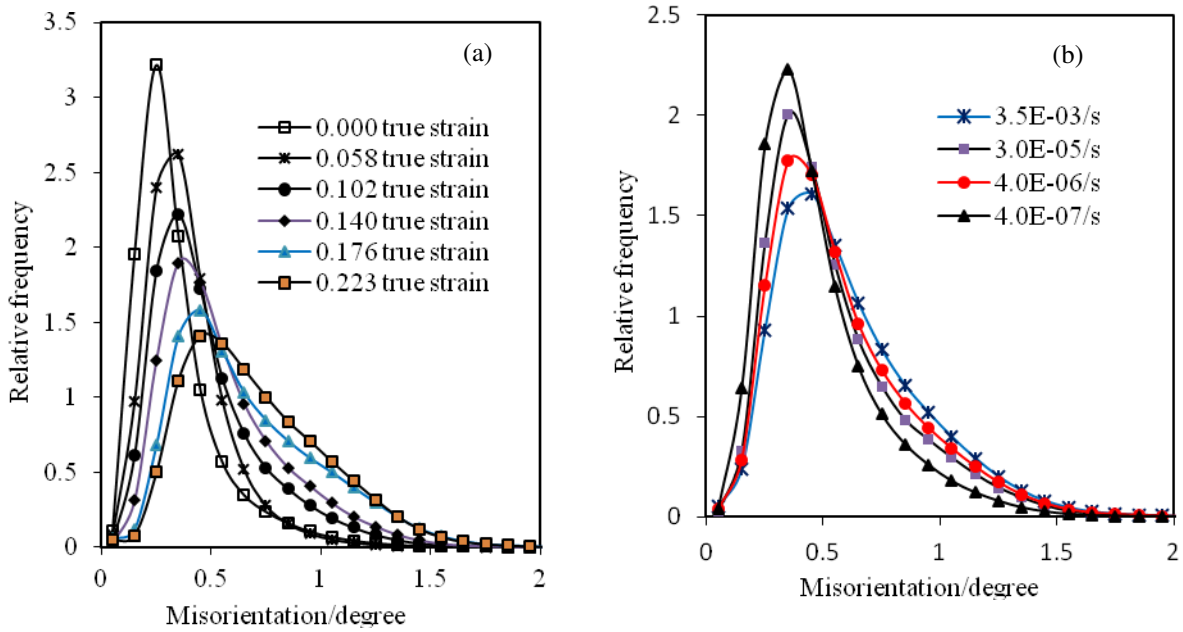

Fig. 11. Misorientation distributions from (a) HTT and (b) HTST tested samples.

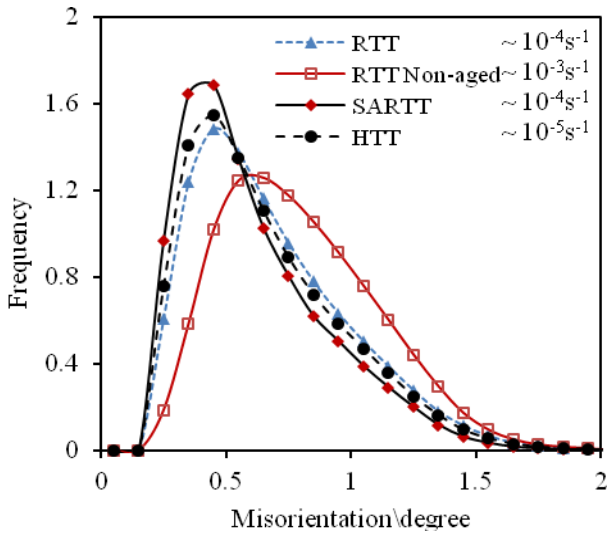

Fig. 12. Misorientation distributions from RTT, RTT-Non-aged, SARTT and HTT tested samples deformed to a true strain of around 0.18.

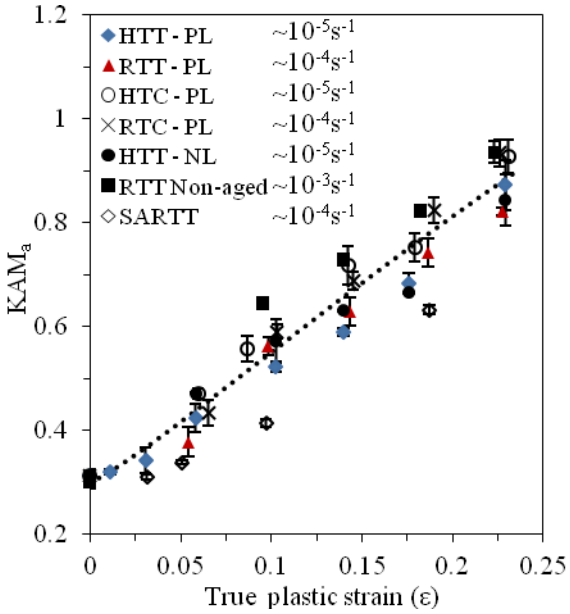

Fig. 13. KAM_a versus true plastic strain for material tested as in Table 1. Experimental data fitted using a Rodbard function. PL: measurement parallel to loading axis, NL: measurement normal to loading axis.

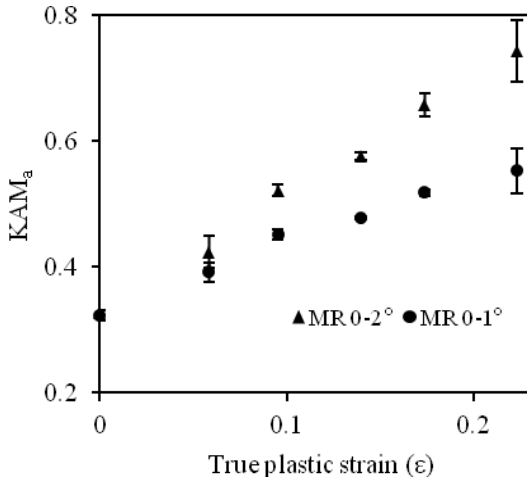

Fig. 14. The effects of the included misorientation range (MR) on KAM_a for HTT tested samples showing increased tendency of KAM_a to saturate at higher strains as MR is reduced.

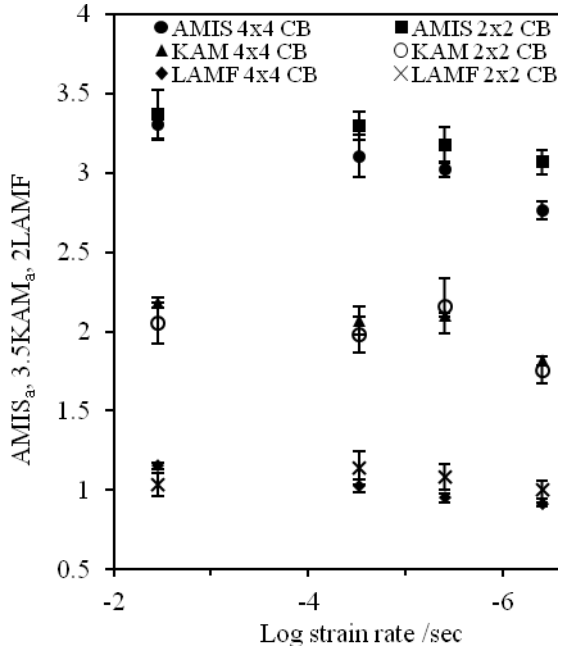

Fig. 15. Strain rate dependence of the $AMIS_a$, KAM_a and LAMF for the HTST tested samples. (CB: EBSD camera binning).

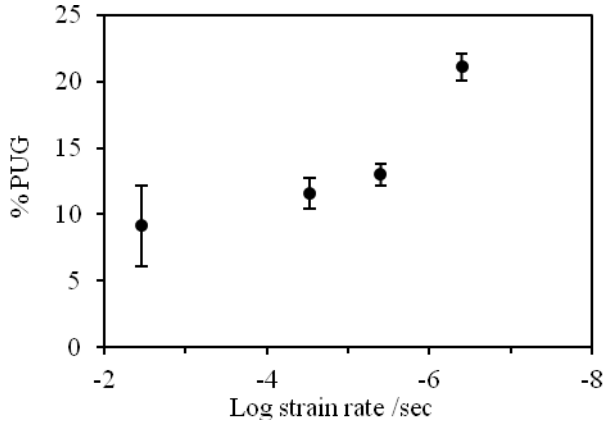

Fig. 16. Proportions of relatively undeformed grains (PUG) versus strain rate for HTST tested samples.

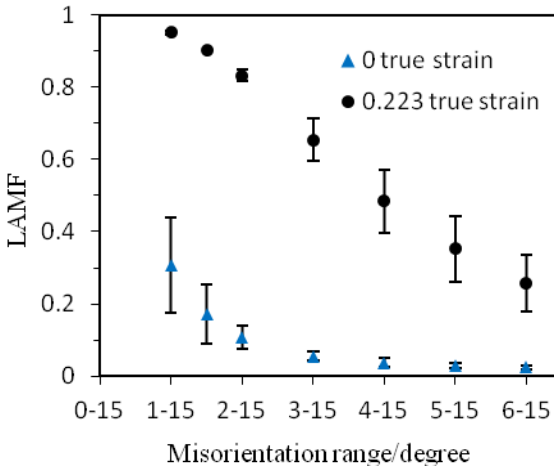

Fig. 17. Change of LAMF as a function of included misorientation range for samples with 0 and 0.223 true strains.

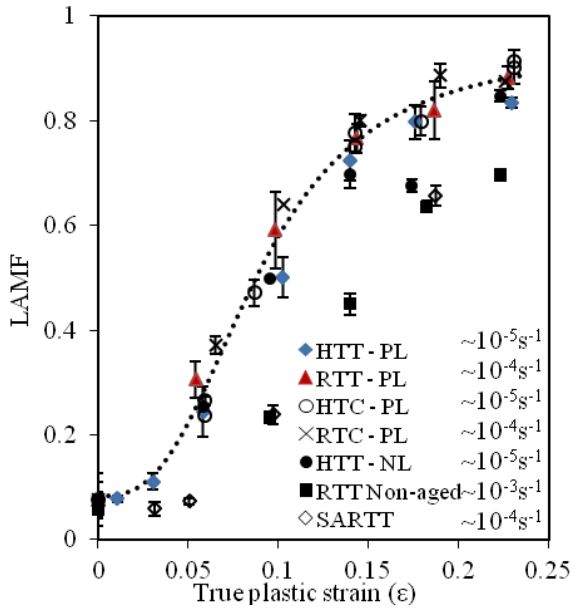

Fig. 18. LAMF versus true plastic strain obtained under conditions stated in Table 1. The experimental data are fitted using a Rodbard function.

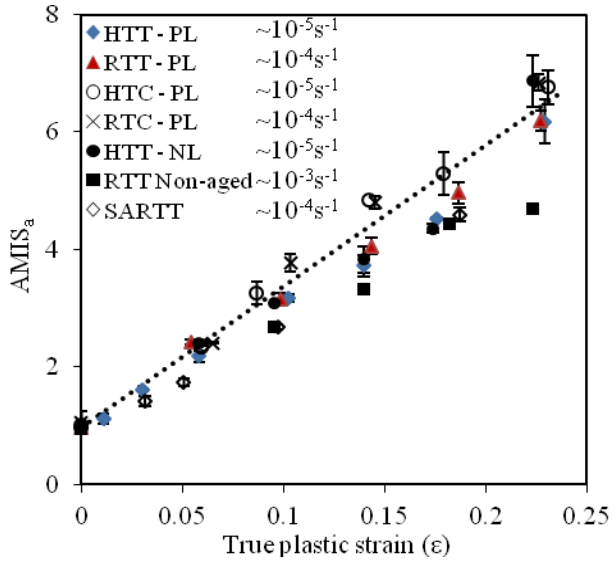

Fig. 19. $AMIS_a$ versus true plastic strain obtained under conditions given in Table 1. (Line fitted by linear regression).

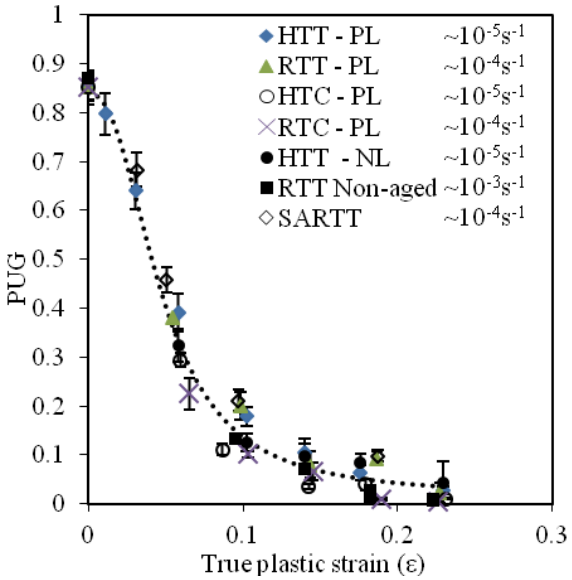

Fig. 20. PUG versus true plastic strain obtained under conditions stated in Table 1. (Line fitted as a Rodbard function).

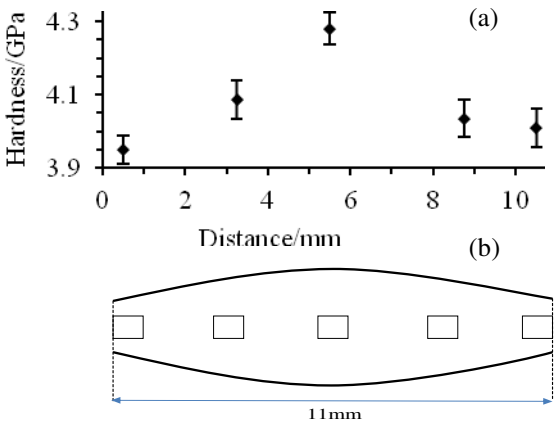

Fig. 21. (a) Hardness profile along the gauge length of a compression specimen deformed to 0.23 true strain at 823K. (b) Schematic representation of the specimen's mid-plane with square grid indicating regions of hardness measurements.

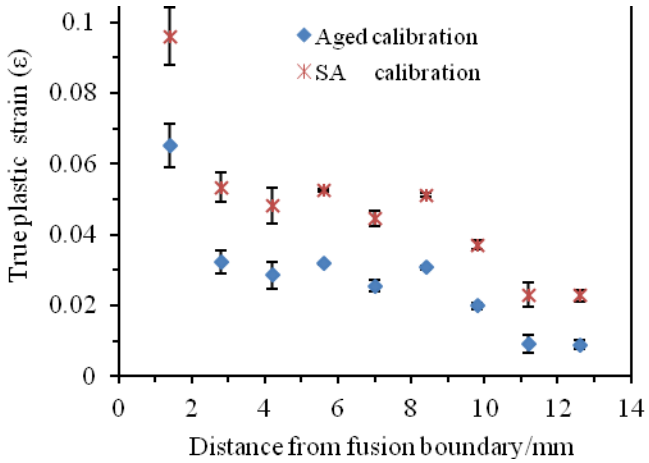

Fig. 22. Strain distribution near the root of an ex-service weld in 316 steel based on calibration curves from aged and solution annealed material.

9. List of Tables

Table 1

Mechanical tests conditions.

Test	True plastic strains (ε)	Strain rate (s^{-1})	Temperature (K)
RTT	0.054, 0.098, 0.143, 0.187, 0.227	$2.0x10^{-4}$	297
HTT	0.011, 0.031, 0.058, 0.102, 0.14, 0.176, 0.223	$3.5x10^{-5}$	823±1
RTC	0.065, 0.081, 0.145, 0.19, 0.226	$5.0x10^{-4}$	297
HTC	0.06, 0.087, 0.142, 0.179, 0.231	$4.0x10^{-5}$	823±1
RTT-Non-aged	0.095, 0.14, 0.182, 0.223	$1.5x10^{-3}$	297
SARTT	0.031, 0.051, 0.097, 0.187	$2.0x10^{-4}$	297
HTST 1	0.098	$3.5x10^{-3}$	823±1
HTST 2	0.098	$3.0x10^{-5}$	823±1
HTST 3	0.098	$4.0x10^{-6}$	823±1
HTST 4	0.098	$4.0x10^{-7}$	823±1

Table 2

EBSD measurement parameters and the associated KAM_a values for the unstrained aged steel (see text for explanation of the abbreviations).

Sample	BD	HR	CB	FA	IR/%	AT/ms	AS/μm	AV/kV	KAM_a
Aged 316H	5-7	60	4x4	4	99	16.2	120	20	0.335
Aged 316H	5-7	80	4x4	4	99	16.2	120	20	0.305
Aged 316H	5-7	100	4x4	4	99	16.2	120	20	0.335
Aged 316H	**5-7**	**120**	**4x4**	**4**	**99**	**16.2**	**120**	**20**	**0.286**
Aged 316H	6-8	120	4x4	4	98.7	16.4	120	20	0.279
Aged 316H	9-11	120	4x4	4	95.8	16.5	120	20	0.268
Aged 316H	3-5	120	4x4	4	99.5	16.2	120	20	0.328
Aged 316H	5-7	120	2x2	4	99.2	72.5	120	20	0.276
Aged 316H	5-7	120	4x4	6	99.1	24.2	120	20	0.280
Aged 316H	5-7	120	4x4	8	99	32.2	120	20	0.283
Aged 316H	5-7	120	4x4	4	99.6	80.6	60	20	0.290
Aged 316H	5-7	120	4x4	4	98.3	16.2	120	17	0.307
Aged 316H	5-7	120	4x4	4	99	32.2	120	15	0.322
Germanium	5-7	120	2x2	4	98	32.4	120	20	0.243
Germanium	5-7	120	4x4	4	98.2	16.1	120	20	0.280